Journal of Alloys and Compounds 1017 (2025) 179048

Contents lists available at ScienceDirect

Journal of Alloys and Compounds

journal homepage: www.elsevier.com/locate/jalcom

Growth and properties of compositionally complex zirconia $Zr_{0.818}(Y_{1/5}Gd_{1/5}Ho_{1/5}Er_{1/5}Yb_{1/5})_{0.182}O_{1.909}$ single crystals

D.A. Agarkov [a], M.A. Borik [b], A.S. Chislov [b,c], B.E. Komarov [b], G.M. Korableva [a], A.V. Kulebyakin [b], I.E. Kuritsyna [a], E.E. Lomonova [b], F.O. Milovich [c,d,*], V.A. Myzina [b], A.A. Reu [b], N.Y. Tabachkova [b,c], M.K. Tapero [b,c], D.M. Zakharov [b,c]

[a] Osipyan Institute of Solid State Physics RAS, Academician Osipyan Str., 2, Chernogolovka 142432, Russia
[b] Prokhorov General Physics Institute of Russian Academy of Sciences, Vavilova Street, 38, Moscow 119991, Russia
[c] Department of Materials Science of Semiconductors and Dielectrics, National University of Science and Technology «MISIS», Leninskiy Prospect, 4, Moscow 119049, Russia
[d] Department of Materials Science, Moscow Polytechnic University, Bolshaya Semyonovskaya Str., 38, Moscow 107023, Russia

ARTICLE INFO

Keywords:
High-entropy oxides
Fluorite structure
Crystal growth
X-ray diffraction pattern
Conductivity

ABSTRACT

Compositionally complex $Zr_{0.818}(Y_{1/5}Gd_{1/5}Ho_{1/5}Er_{1/5}Yb_{1/5})_{0.182}O_{1.909}$ single crystals were grown for the first time using directional melt crystallization in a cold crucible. The phase composition and structure of single crystals have been studied using X-ray diffraction, Raman spectroscopy, and transmission electron microscopy. The conductivity of the crystals was studied using impedance spectroscopy in the 350 – 900 °C temperature range. The structure and properties of $Zr_{0.818}(Y_{1/5}Gd_{1/5}Ho_{1/5}Er_{1/5}Yb_{1/5})_{0.182}O_{1.909}$ single crystals were compared with those of binary solid solution $Zr_{0.818}R_{0.182}O_{1.909}$ single crystals (R = Y, Gd, Yb, Ho, Er). The as-grown crystals proved to have almost homogeneous lengthwise component distributions. The compositionally complex $Zr_{0.818}(Y_{1/5}Gd_{1/5}Ho_{1/5}Er_{1/5}Yb_{1/5})_{0.182}O_{1.909}$ single crystals have a pseudocubic t'' phase structure and high structural perfection. The lattice parameter of multicomponent $Zr_{0.818}(Y_{1/5}Gd_{1/5}Ho_{1/5}Er_{1/5}Yb_{1/5})_{0.182}O_{1.909}$ single crystals fits well to linear dependence of lattice parameter on the stabilizing ion radius in $Zr_{0.818}R_{0.182}O_{1.909}$ crystals. The conductivity of $Zr_{0.818}(Y_{1/5}Gd_{1/5}Ho_{1/5}Er_{1/5}Yb_{1/5})_{0.182}O_{1.909}$ single crystals also agrees well with the dependence of conductivity on ionic radius of the stabilizer in $Zr_{0.818}R_{0.182}O_{1.909}$ crystals. The specific high-temperature conductivity of $Zr_{0.818}(Y_{1/5}Gd_{1/5}Ho_{1/5}Er_{1/5}Yb_{1/5})_{0.182}O_{1.909}$ single crystals is comparable to the specific conductivity of the $Zr_{0.818}R_{0.182}O_{1.909}$ single crystals. The results of this work show that for the $Zr_{0.818}(Y_{1/5}Gd_{1/5}Ho_{1/5}Er_{1/5}Yb_{1/5})_{0.182}O_{1.909}$ multicomponent single crystals, the geometry factor predominates over the entropy factor.

1. Introduction

The development of new approaches to the design of materials having unique properties and the search for new advanced synthesis techniques favor the progress of materials science. One example of these approaches is the development of high-entropy materials (HEM) concept. This approach was initially implemented for high-entropy or multicomponent alloys [1–5], but the family of HEM has broadened considerably by now, in particular compositionally complex oxides, including are high-entropy oxide materials (HEOs) [6–15].

The main advantage of HEM is the possibility to significantly broaden the range of their compositions and to control and improve their performance. However, the large number of possible component combinations in high-entropy compounds greatly complicates the prediction of their structural and physicochemical properties.

When considering the development prospects of new HEM one should bear in mind the necessity of additional studies [15]. These include, for example, assessment of the most important factors controlling the formation of stable HEOs; behavior and properties of single HEO components and their effect on the crystalline structure; identification of additional factors (except high entropy) that determine phase formation; theoretical studies of the interrelation between the chemical

* Corresponding author at: Department of Materials Science of Semiconductors and Dielectrics, National University of Science and Technology «MISIS», Leninskiy Prospect, 4, Moscow 119049, Russia.
E-mail address: philippmilovich@gmail.com (F.O. Milovich).

https://doi.org/10.1016/j.jallcom.2025.179048
Received 16 November 2024; Received in revised form 14 January 2025; Accepted 6 February 2025
Available online 7 February 2025

composition and properties of these materials. Solving the above questions is required for the development of materials exhibiting optimum properties for specific applications [15].

Special attention is paid to HEOs having a fluorite structure which are a very important family of functional ceramic materials [12–16]. Some guidelines to synthesizing HEOs having a fluorite structure and containing rare-earth element oxides in equimolar quantities have been set forth as follows: the ionic radii of all the constituent cations are close; at least one of the constituent oxides has a crystalline structure differing from the others; at least one cation does not have any miscibility on the binary phase diagram [14]. It has also been stressed that, along with high entropy, oxide vacancies forming upon the heterovalent substitution in the solid solutions also favor the stability of the fluorite phase in these materials. For example, the stability of fluorite HEOs increases upon the introduction of bivalent Ca^{2+} cations since the number of forming oxygen vacancies is greater than upon the introduction of a trivalent R^{3+} cation [15]. A model based on the size and ionic radii ratio of the constituent elements and allowing one to predict the structure of the solid solutions was suggested [17]. The geometrical and statistical criteria of the formation of single-phase fluorite and bixbyite solid solutions were analyzed in the latter cited work based on a systematic study of 18 equimolar 5-component specimens containing rare-earth oxides.

Zirconia, hafnia and ceria based fluorite-structure materials are widely used as solid state electrolytes in electrochemical devices, thermal barrier coatings, gas sensors, oxygen pumps, biomarkers, memristors, catalysts etc. There is great interest in the search for new materials having low thermal conductivity and high strength for potential applications such as thermal barrier coatings in gas turbine and rocket engines etc. in which yttria stabilized zirconia (YSZ) is typically used. High-entropy YSZ ceramics are studied for improving the mechanical strength and wear resistance and reducing the thermal conductivity of the coatings [15,16,18]. Great attention is also paid to zirconia (hafnia or ceria) based solid state electrolytes that have high oxygen ion conductivity (0.01 S/m at 600 °C) [19]. Their high ionic conductivity originates from the presence of oxygen vacancies in zirconia based solid solutions that compensate charge upon the heterovalent substitution of the parent Zr^{4+} cations for the trivalent R^{3+} of the stabilizing oxide. The electrical conductivity of several high-entropy fluoride structure oxides was studied [20]. The specimens had lower electrical conductivity than Y_2O_3-stabilized ZrO_2. It was hypothesized that the lower conductivity originated from a non-optimum overall content of the stabilizing oxides, the presence of CaO and the high grain-boundary resistivity caused by small grain sizes of the HEOs due to low grain growth rate. Another study of the electric transport parameters of 8 mol% $(Sc_{0.2}Lu_{0.2}Yb_{0.2}Y_{0.2}Dy_{0.2})$–$ZrO_2$ ceramics also showed a decrease in the ionic conductivity of the ceramics as compared to 8YSZ specimens. However, the multicomponent ceramics exhibited lower susceptibility to conductivity degradation upon long term high temperature treatment than 8YSZ ceramics [21].

There are recent publications on the growth of single-phase high-entropy oxide bulk single crystals having different structural types, e.g., rare-earth garnets [22,23], rare-earth monoclinic aluminates [24], rare-earth pyrochlore titanates [25,26], rare-earth perovskites [27], rare-earth oxides [28] and transition metal ortoferrites [29].

Earlier we synthesized and studied binary $Zr_{0.818}R_{0.182}O_{1.909}$ solid solution single crystals where R = Y, Gd, Yb. The content of trivalent cation oxides (R_2O_3) in the test crystals was 10 mol.%. The crystals were single-phase and had a fluorite cubic structure [30]. It can be assumed that single-phase solid solution single crystals with a fluorite structure can also be synthesized for multicomponent compositions. There is no literary data thereon. The criterion for selecting the test composition was a 10 mol.% overall concentration of stabilizing oxides, i.e., the stabilizing oxide content required for the formation of a fluorite cubic solid solution. Furthermore, each of the 5 selected stabilizing oxides also formed a fluorite cubic solid solution at 10 mol.% concentration.

The aim of this work was to synthesize compositionally complex $Zr_{0.818}(Y_{1/5}Gd_{1/5}Ho_{1/5}Er_{1/5}Yb_{1/5})_{0.182}O_{1.909}$ single crystals and study their structure and transport properties. The ionic radii of Y^{3+}, Gd^{3+}, Ho^{3+}, Er^{3+} and Yb^{3+} rare-earth cations for a coordination number of 8 are 1.019, 1.053, 1.015, 1.004 and 0.985 Å, respectively [31]. Furthermore, $Zr_{0.818}R_{0.182}O_{1.909}$ (R = Ho, Er) single crystals were synthesized. The structure and properties of the $Zr_{0.818}(Y_{1/5}Gd_{1/5}Ho_{1/5}Er_{1/5}Yb_{1/5})_{0.182}O_{1.909}$ single crystals were compared to those of $Zr_{0.818}R_{0.182}O_{1.909}$ binary solid solution single crystals (R = Y, Gd, Ho, Er, Yb) for detecting possible effect of the compositional factor.

2. Experimental

$Zr_{0.818}(Y_{1/5}Gd_{1/5}Ho_{1/5}Er_{1/5}Yb_{1/5})_{0.182}O_{1.909}$ single crystals were grown using directional melt crystallization in a cold crucible by direct high frequency melting. The high frequency lamp generator had a 63 kW power and 5.28 MHz frequency. Powdered oxides were mixed in the required ratio in a 90 mm diam. water-cooled copper crucible. The crucible was made from U-shaped copper tubes mounted on a dielectric basement. The charge powder weight was ~2.8 kg. Fig. 1 shows schematic representation of the main heating unit components. Melting was initiated by introducing 5 – 7 g metallic Zr fragments into the charge powder mixture. More oxide mixture was added to the crucible as the melted volume increased. Direction crystallization was carried out by moving the melt out of the highest temperature zone at a specified speed. Practically, the crucible was lowered relative to the induction coil at an 8 mm/h speed. The high frequency generator was switched off after the completion of crystallization. The resultant ingot consisted of coalesced discrete single crystals which were then mechanically separated and used for making the test specimens.

A more detailed description of the theoretical and practical aspects of applying this method to the growth of zirconia based single crystals is available elsewhere [32].

The phase composition of the crystals was studied using X-ray diffraction and Raman spectroscopy. The X-ray diffraction study of phase composition and structure was conducted on a BrukerD8 diffractometer in $Cu_{K\alpha}$ radiation in 40 kV and 40 mA mode. The phase composition of the crystals was studied with a standard method used for single crystals. The as-grown crystals had no predominant crystallographic orientation and therefore each crystal was preliminarily oriented in the diffractometer relative to specific crystallographic

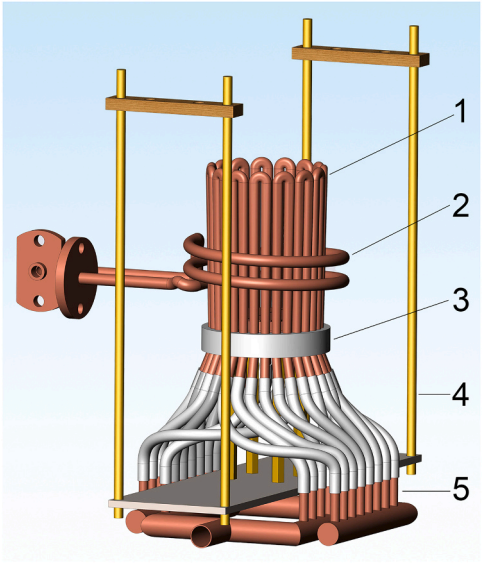

Fig. 1. Schematic of crystal growth heating unit components: (1) crucible, (2) induction coil, (3) crucible basement, (4) crucible movement system fastening rods and (5) water manifold.

directions. The test specimens were cut from the middle parts of the crystals. The wafers for the phase composition study were cut from the crystals perpendicular to the < 100 > direction. The 2θ measurement range was 20–140 arc deg at a 0.02 deg step.

Raman spectroscopy phase analysis was conducted in the 100–800 cm^{-1} wavenumber range under a Renishaw inVia confocal Raman microscope with a 532 nm exciting laser.

The absorption spectra were recorded with a Cary 5000 two-beam spectrophotometer in the 200 – 800 nm wavelength range.

The lengthwise solid solution component distributions were studied by energy dispersion analysis with a JEOL 5910 LV (Japan) scanning electron microscope equipped with an X-MAX 80 (EDX: SDD detector - 80 mm^2 active area) energy dispersive system from Oxford Instruments, England. The measurements were carried out on polished plates cut along the direction of crystal growth in 1 mm increments.

The structure of the crystals was studied using transmission electron microscopy (TEM) under a JEM 2100 microscope (Japan) at a 200 kV accelerating voltage. The test specimens were made with a focused ion beam.

The electric conductivity of the crystals were studied using a four-probe method in the 350 – 900 °C temperature range at a 50 °C step with a Solartron SI 1260 frequency analyzer in the 0.1 Hz – 5 MHz range. The AC bias signal amplitude was 24 mV. The impedance spectra were processed with the ZView software ver. 2.8. The test specimens for the electrical measurements were in the form of single crystal 500 μm thick wafers sized 7 × 7 mm.

3. Results and discussion

Fig. 2 shows the general appearance of the as-grown $Zr_{0.818}(Y_{1/5}Gd_{1/5}Ho_{1/5}Er_{1/5}Yb_{1/5})_{0.182}O_{1.909}$ single crystals. The crystals have columnar shapes that are typical of the crystals grown using directional melt crystallization in a cold crucible. The crystals were 10–15 mm in cross-section and up to 40 mm in length. The shapes and sizes of the crystals were substantially like those of earlier grown $Zr_{0.818}R_{0.182}O_{1.909}$ binary solid solution crystals (R = Y, Gd, Yb) [30].

The overall concentration of the stabilizing oxides in the compositionally complex $Zr_{0.818}(Y_{1/5}Gd_{1/5}Ho_{1/5}Er_{1/5}Yb_{1/5})_{0.182}O_{1.909}$ single crystals was 10 mol.%, hence the crystals are hereinafter denoted as 10(Y,Gd,Ho,Er,Yb)SZ. The $Zr_{0.818}Yb_{0.182}O_{1.909}$, $Zr_{0.818}Y_{0.182}O_{1.909}$, $Zr_{0.818}Gd_{0.182}O_{1.909}$, $Zr_{0.818}Ho_{0.182}O_{1.909}$ and $Zr_{0.818}Er_{0.182}O_{1.909}$ binary solid solution crystals are denoted as 10YbSZ, 10YSZ, 10GdSZ, 10HoSZ and 10ErSZ, respectively. The as-grown 10(Y,Gd,Ho,Er,Yb)SZ crystals were homogeneous and transparent which indirectly indicates their monophasic nature and the absence of macrodefects (inclusions, pores, cracks) in the volume of the crystals. The appearance of the crystals was similar to that of single-phase two-component cubic zirconia crystals.

The 10(Y,Gd,Ho,Er,Yb)SZ crystals changed color when illuminated with different sources. In daylight or under an incandescent light the crystals were yellow (Fig. 2a) whereas in luminescent light their color became pink (Fig. 2b). This color behavior is caused by the presence of narrow absorption bands in the visible spectral region, i.e., the Ho^{3+} band (the 418, 453, 485, 538 and 642 nm peaks) [33] and the Er^{3+} band (the 378, 412, 449, 482, 520, 564 and 648 nm peaks) [34] (Fig. 3). Similar color-change behavior depending on illumination spectrum was observed for ZrO_2–Y_2O_3 solid solution crystals additionally doped with Ho_2O_3 [35]. The latter crystals were pale yellow-green in daylight whereas under luminescent illumination by an F9 source (CIE standard) the crystals became green-blue and changed to purple-violet under luminescent illumination by an F10 source. The above color-change phenomena originate from the specific combination of the visible region absorption spectrum of the crystals and the spectral parameters of

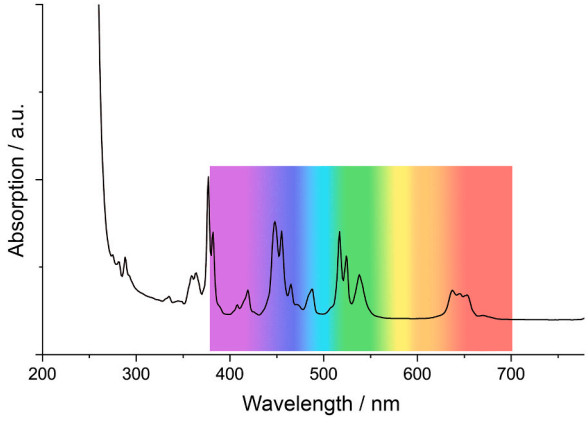

Fig. 3. Absorption spectrum of $Zr_{0.818}(Y_{1/5}Gd_{1/5}Ho_{1/5}Er_{1/5}Yb_{1/5})_{0.182}O_{1.909}$ crystals.

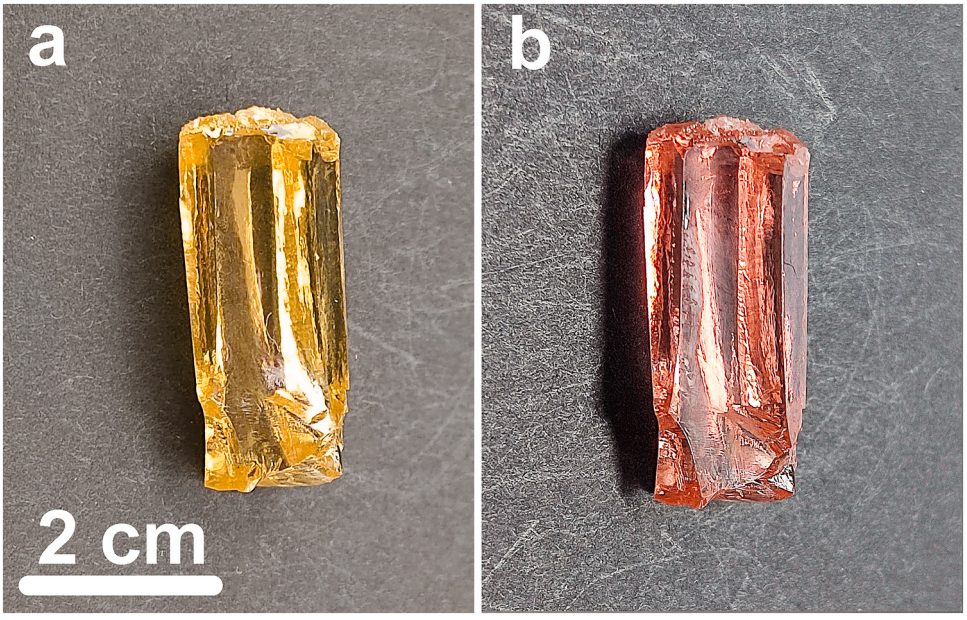

Fig. 2. Appearance of $Zr_{0.818}(Y_{1/5}Gd_{1/5}Ho_{1/5}Er_{1/5}Yb_{1/5})_{0.182}O_{1.909}$ crystals (a) in daylight and (b) in luminescent light.

the light sources.

The compositional homogeneity of the 10(Y,Gd,Ho,Er,Yb)SZ solid solution crystal was assessed from the distribution of components along the length of the crystal (Fig. 4). As can be seen from Fig. 4, the 10(Y,Gd,Ho,Er,Yb)SZ crystals have almost homogeneous ZrO_2, Y_2O_3, Ho_2O_3 and Er_2O_3 distributions with a slight decrease in the concentrations of the latter three oxides toward the end of the crystal. This indicates that the effective distribution coefficients of these oxides is equal to or slightly greater than 1 for directional melt crystallization, which is consistent with previously published data [32]. The distributions of Gd_2O_3 and Yb_2O_3 are more inhomogeneous. The Yb_2O_3 concentration profile pattern is similar to that observed for Y_2O_3, Ho_2O_3, and Er_2O_3 but it is more pronounced. In the case of Gd_2O_3, there is a clear trend towards an increase in concentration along the length of the crystal. This indicates that the effective distribution coefficient of Gd_2O_3 is less than 1. It is interesting to note that the two components with the largest and smallest ionic radii among the five trivalent oxides, Gd_2O_3 and Yb_2O_3 respectively, exhibit the greatest deviations from a uniform distribution.

Fig. 5 shows X-ray diffraction patterns for the 10(Y,Gd,Ho,Er,Yb)SZ single crystals and for the powdered crystals. Analysis of the X-ray data suggests that the 10(Y,Gd,Ho,Er,Yb)SZ crystals had a fluorite cubic structure with lattice parameter equal to 5,1438(1) Å. The phase composition and lattice parameter of the crystals did not change after grinding. The powders and the single crystals contained only the cubic ZrO_2 modification with lattice parameter equal to 5144(1) Å. The width of the rocking curve (FWHM) of the 10(Y,Gd,Ho,Er,Yb)SZ crystal was ~ 0.07 deg in low resolution for the (006) reflection. This is comparable with the FWHM for the binary $Zr_{0.818}R_{0.182}O_{1.909}$ crystals which is 0.06 – 0.08 deg. Thus, modifying the composition by increasing the number of components in the compound does not result in a decrease in the structural perfection of the single crystals when using this growth method.

One of the most important parameters determining the possibility of forming HEOs with a fluorite structure is the average radius of their constituent cations [36]. Therefore, it is interesting to compare the lattice parameters of the multicomponent 10(Y,Gd,Ho,Er,Yb)SZ crystals with previously published data on the lattice parameters of binary system single crystals 10YbSZ, 10YSZ, and 10GdSZ [30], as well as the 10HoSZ and 10ErSZ crystals obtained in this study. Such comparison seems to be correct, since the crystals were obtained by directional melt crystallization under the same temperature and time synthesis conditions, with the content of stabilizing oxide being the same in each crystal (including the compositionally complex crystal) and amounting to 10 mol.%. Fig. 6 shows the lattice parameter of the 10YbSZ, 10YSZ, 10GdSZ, 10HoSZ and 10ErSZ and 10(Y,Gd,Ho,Er,Yb)SZ crystals as a function ionic radius of stabilizing cation. The values of the ionic radii of rare-earth cations for the coordination number 8 are given in accordance with [31]. The calculated average ionic radius of the trivalent cations for the 10(Y,Gd,Ho,Er,Yb)SZ crystals is about 1.0152 Å.

The dependence of the lattice parameters on the ionic radius of the stabilizing cation is linear, and it increases with increasing ionic radius of the rare earth cation. The data for the compositionally complex 10(Y,Gd,Ho,Er,Yb)SZ crystal fits well into this dependence. Thus, the lattice parameters of multicomponent single-phase fluorite cubic zirconia crystals can be predicted based on their composition and the ionic radii of their constituent trivalent cations.

The phase composition of the crystals was also studied using Raman spectroscopy. Fig. 7 shows the Raman spectra of the 10 (Y,Gd,Ho,Er,Yb) SZ crystal, as well as 10YbSZ, 10YSZ, HoSZ, and 10GdSZ crystals, for comparison. The Raman spectra of the 10ErSZ crystals were not provided, as the use of a laser with a wavelength of 532 nm as an excitation source led to the excitation of luminescence bands of the Er^{3+} ion. This made it difficult to accurately interpret the results.

A distinctive feature of the Raman spectrum of the compositionally complex 10(Y,Gd,Ho,Er,Yb)SZ crystal compared to binary single crystals is a notably wider band in the region ~600 cm^{-1}. This band broadening is likely due to an increase in disorder in the solid solution due to the presence of different rare-earth cations in the crystal lattice [37]. The frequency of vibrations within a crystal lattice is primarily determined by the strength of the bonds between neighboring atoms, the distance between participating ions, and the mass of the ions involved. A stronger bond results in a higher oscillation frequency compared to a weaker bond. A shorter distance between participating ions or Zr^{4+} ion substitution for a heavier one cause a high-frequency shift. The study of the

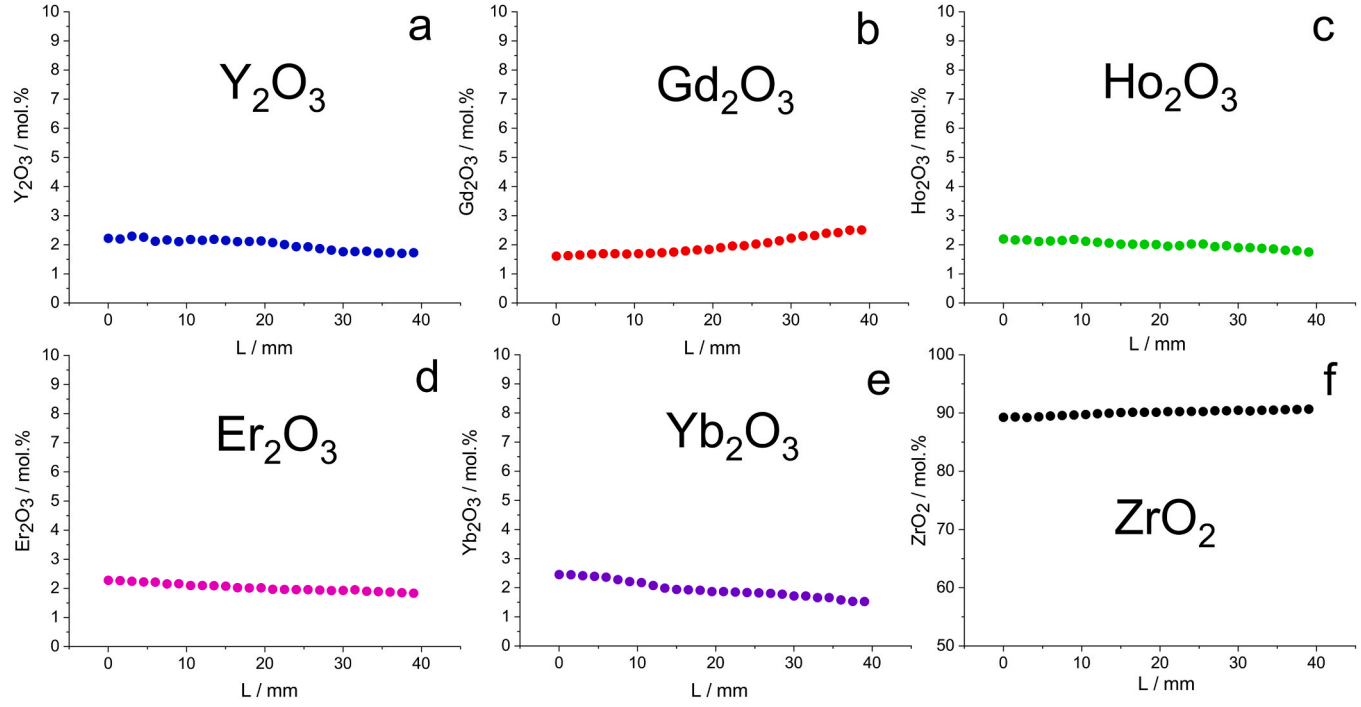

Fig. 4. Component profiles in the length of $Zr_{0.818}(Y_{1/5}Gd_{1/5}Ho_{1/5}Er_{1/5}Yb_{1/5})_{0.182}O_{1.909}$ solid solution crystal. a – Y_2O_3, b– Gd_2O_3, c – Ho_2O_3, d – Er_2O_3, e – Yb_2O_3, f – ZrO_2.

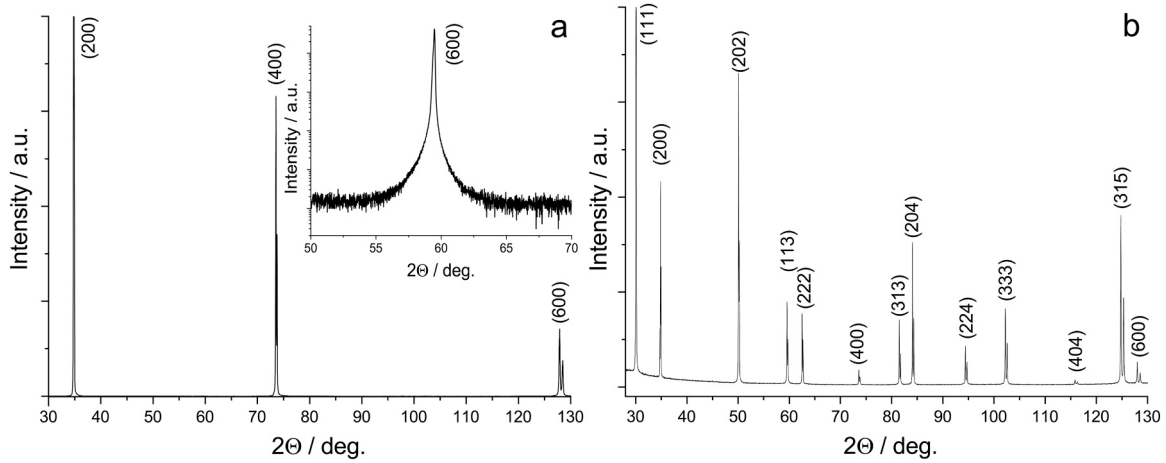

Fig. 5. X-ray diffraction patterns (a) for wafer cut from $Zr_{0.818}(Y_{1/5}Gd_{1/5}Ho_{1/5}Er_{1/5}Yb_{1/5})_{0.182}O_{1.909}$ crystal perpendicular to the < 001 > direction and (b) for powdered crystal. Insert shows (006) reflection rocking curve.

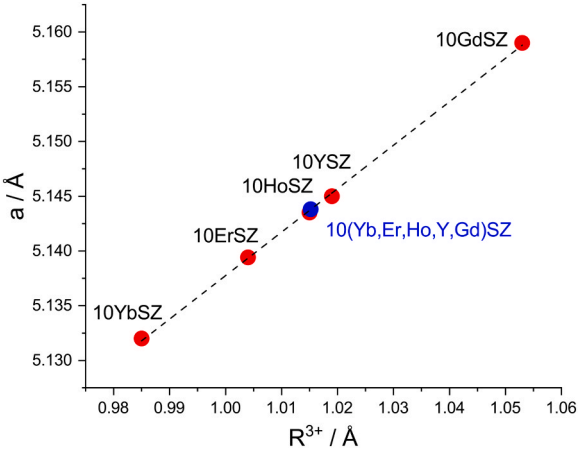

Fig. 6. Crystal lattice parameter as a function of stabilizing cation ionic radius.

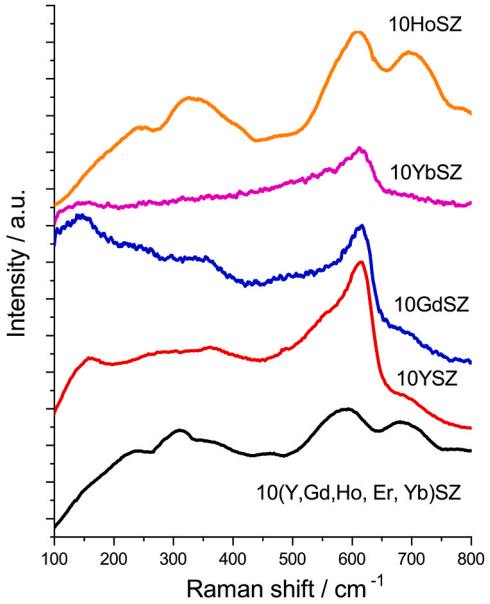

Fig. 7. Raman spectra of 10(Y,Gd,Ho,Er,Yb)SZ, 10YbSZ, 10YSZ, 10GdSZ and HoSZ crystals.

oscillation modes of tetragonal and cubic phases in the ZrO_2-Y_2O_3 system [38] reveals that the shifts of both the F_{2g} cubic mode and the A_{1g} and E_g tetragonal ones is linked to an elongation of the Zr-O_I bond in the corresponding ZrO_2 lattice. The shift of the Zr-O_I band in the 10(Y,Gd, Ho,Er,Yb)SZ crystals is influenced by a change in the crystal lattice parameter, Zr^{4+} replacement of Zr^{4+} ions with rare earth element cations of different weights, and a change in the Zr-O_I bond strength due to the effect on the local structure of various doping cations. The latter factor is caused by different positions of the oxygen vacancies relative to trivalent stabilizing oxide cations and host Zr^{4+} cation. If the coordination number of the Zr^{4+} cation changes from 8 to 7, the bond between the Zr ion and the seven remaining O^{2-} ions becomes stronger and hence the ZrO_7 binding energy is significantly higher [38]. Thus, the additive effect of multiple doping cations with different weights and radii on the local structure has led to a significant broadening of the band in the region ~600 cm^{-1}. It should be noted that in the spectrum of 10(Y,Gd, Ho,Er,Yb)SZ crystals, a band at ~ 470 cm^{-1} is observed which is characteristic of the tetragonal t'' phase of zirconia [38]. It has been shown in several papers that the tetragonal t`` and cubic phases have almost the same lattice parameters, but they belong to different space groups ($P4_2/mnc$ and Fm3m, respectively). These structural differences are caused by the slight displacement of oxygen ions in relation to the ideal positions of the anionic fluorite sublattice [39,40]. The Raman spectroscopy method is sensitive to oxygen displacements due to its high polarizability. This is why it is often used for studying the structure of materials based on zirconium dioxide. The t'' phase was observed in molten and quenched YSZ specimens [39], thermal barrier coatings [40] and solid electrolyte films [41]. Raman spectra of the (8−10)YSZ crystals grown by directional crystallization in a cold crucible were also observed to contain a peak in the vicinity of 470 cm^{-1} which was absent in crystals with yttrium oxide concentrations of 12–20 mol% Y_2O_3 [42].

Transmission electron microscopy and electron diffraction techniques were used to refine the crystal structure of 10(Y,Gd,Ho,Er,Yb)SZ multicomponent crystals. Due to the fact that the amplitude of electron scattering is four orders of magnitude larger than that of X-rays, electron diffraction allows for a more accurate determination of the position of light atoms within a unit cell that contains heavy atoms. To distinguish between the cubic and tetragonal symmetries of the crystal lattice of zirconium dioxide, the < 111 > and < 110 > axes are traditionally used. The presence or absence of certain reflections, such as {112} and {011}, on electronograms can indicate whether the crystal has tetragonal symmetry or not [43,44].

Fig. 8 shows the TEM images and electron diffraction patterns of the 10(Y,Gd,Ho,Er,Yb)SZ crystals.

The electron diffraction patterns of the 10(Y,Gd,Ho,Er,Yb)SZ crystal

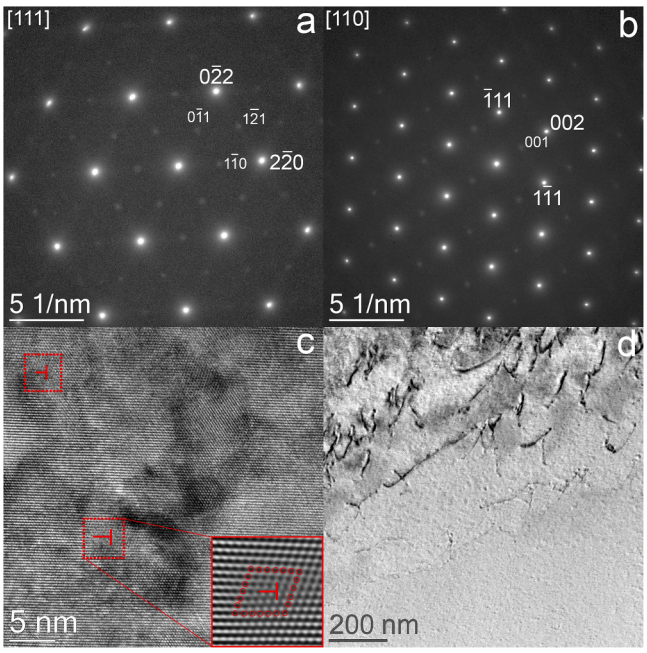

Fig. 8. Electron diffraction patterns (a, b) and TEM images (c, d) of $Zr_{0.818}(Y_{1/5}Gd_{1/5}Ho_{1/5}Er_{1/5}Yb_{1/5})_{0.182}O_{1.909}$ crystal.

specimens cut perpendicular to the < 111 > and < 110 > axis contain weak (110) and (112) type reflections (Fig. 8a) and (100) and (110) type reflections (Fig. 8b). The presence of these reflections suggests that the structure of these crystals is tetragonal ($P4_2/mnc$ space group) which is consistent with Raman spectroscopy data.

The TEM structural images of crystals show discrete dislocations (Fig. 8c,d). A similar defect structure was observed in high-entropy ($Sc_{0.2}Lu_{0.2}Yb_{0.2}Y_{0.2}Dy_{0.2}$)–$ZrO_2$ crystals [21]. No dislocations were detected in the structure of binary $Zr_{0.818}R_{0.182}O_{1.909}$ crystals by the TEM method. The dislocation density in $Zr_{0.818}Y_{0.182}O_{1.909}$ crystals was approximately 10^3 cm^{-2} as measured by optical microscopy using etching pits. The low dislocation density is due to the presence of ionic bonds, which is characteristic of oxide materials, and in particular solid solutions based on zirconia. An estimate of the dislocation density in a multicomponent 10(Y,Gd,Ho,Er,Yb)SZ crystal yields a value of 10^9 cm^{-2}, which is much more than in crystals of binary systems. The study of the dislocation structure in ceramic high-entropy oxide materials has revealed that the dislocation density is highly dependent on the number of constituent elements in the composition. It has been demonstrated through molecular dynamic simulation methods that the energy change caused by the presence of edge dislocations can be offset by an increase in the configurational entropy, leading to thermodynamic stability. It has been reported that the density of dislocations, which are evenly distributed throughout the volume of compositional complex ceramics, can reach 10^9 MM^{-2} [45]. In the same article, it was demonstrated that the presence of high-density dislocations in oxide ceramics provides an additional hardening mechanism, leading to improved mechanical strength. As demonstrated in the current study, an increase in the number of components in fluorite solid solutions also leads to a substantial increase in the density of edge dislocations.

Thus, the use of Raman spectroscopy and electron diffraction techniques has made it possible to refine the structure of multicomponent 10(Y,Gd,Ho,Er,Yb)SZ crystals and to show that they have a tetragonal t`` phase structure, rather than the cubic structure that was suggested by X-ray diffraction results.

Fig. 9 shows the typical impedance spectra of the 10(Y,Gd,Ho,Er,Yb)SZ crystals in Nyquist coordinates at 400 and 900 °C. The low-temperature regions of the impedance spectra (350–400 °C) can be divided into two sections: a high-frequency section corresponding to the bulk resistivity of the test specimen, and a low-frequency region corresponding to the electrode impedance of the electrode/electrolyte interface (Fig. 9a). The high-frequency section of the impedance spectrum is a perfect arc centered almost exactly on the real resistivity axis. The impedance spectra were fitted with an equivalent electrical circuit (R_b-CPE_b) consisting of a resistor (R_b) connected in parallel with a constant phase element (CPE_b). The exponent CPE_b was approximately 0.85–0.95. The low-frequency arc corresponds to the polarization impedance of the electrode/electrolyte boundary. At higher temperatures (Fig. 9b) the impedance spectrum pattern changes to contain an inductive "tail" showing itself in the high-frequency spectrum region, corresponding to the inductive contribution from the current conductors and an arc, corresponding to reversible electrode processes at the electrode/electrolyte boundary. The high-temperature impedance spectra were fitted with an equivalent electrical circuit $LR_b(R_{electrode}$-$CPE_{electrode})$ consisting of sequence-connected elements corresponding to the inductance of the current conductors (L), the electrolyte bulk resistivity (R_b) and the electrode contribution from the electrode/electrolyte boundary, the latter being connected in parallel to a constant phase element ($R_{electrode}$-$CPE_{electrode}$).

Fig. 10 shows the conductivity *vs* temperature curves for the 10(Y,Gd,Ho,Er,Yb)SZ, 10YbSZ, 10YSZ, 10GdSZ, 10HoSZ, and 10ErSZ crystals in Arrhenius coordinates.

The conductivity *vs* temperature plots for all the specimens, except 10GdSZ, exhibit visible curvature. The observed change in the curve slope suggests a change in the conductivity activation energy in different temperature ranges and can be caused by destruction of local defect clusters at high temperatures [46]. Note that the temperature plot for the specific electrical conductivity plot for 10(Y,Gd,Ho,Er,Yb)SZ crystals almost coincides with that of 10HoSZ.

Fig. 11 illustrates the values of crystal conductivity at 850 °C, depending on the ionic radius of the stabilizing cation. The conductivity of crystals decreases as the ionic radius of the stabilizing cation increases. This trend is also seen in the case of 10(Y,Gd,Ho,Er,Yb)SZ

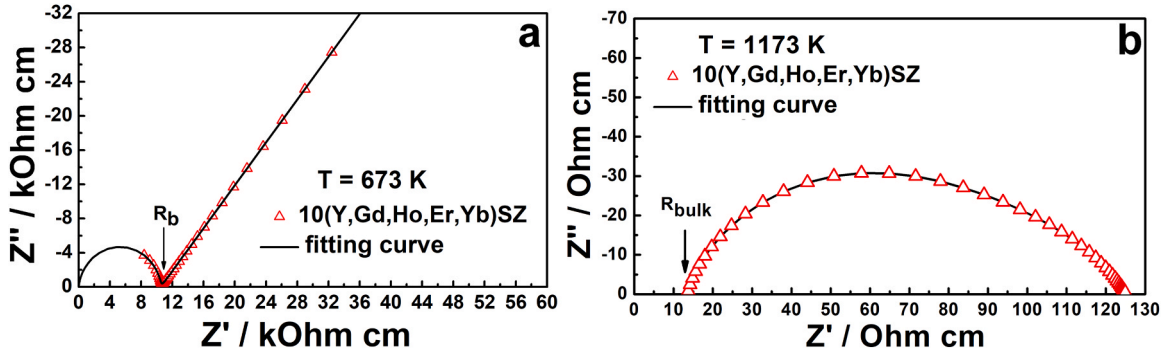

Fig. 9. Impedance spectra in Nyquist coordinates for 10(Y,Gd,Ho,Er,Yb)SZ single crystal at (a) 673 K and (b) 1173 K.

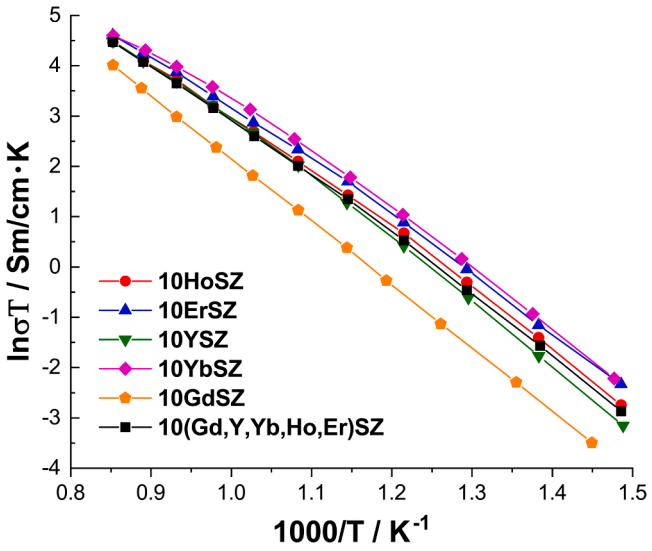

Fig. 10. Arrhenius plots for the conductivity of 10(Y,Gd,Ho,Er,Yb)SZ, 10YbSZ, 10YSZ, 10GdSZ, 10HoSZ and 10ErSZ crystals.

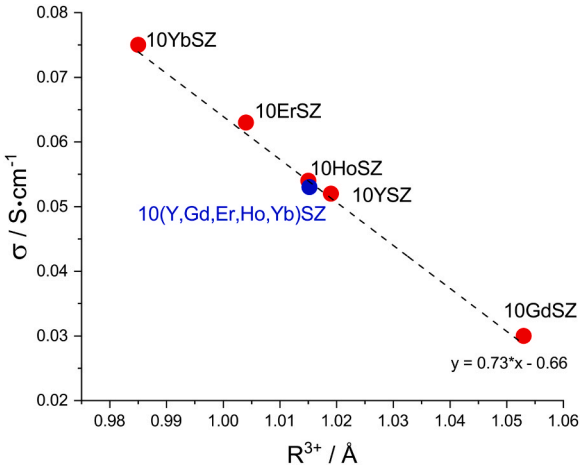

Fig. 11. Conductivity of the crystals at 850 °C as a function of stabilizing cation ionic radius.

crystal. (The average rare-earth cation radius was used for the 10(Y,Gd,Ho,Er,Yb)SZ crystals.)

Thus, the electrical conductivity of the compositionally complex 10(Y,Gd,Ho,Er,Yb)SZ crystal differs slightly from that of the conventional solid state electrolytes (YSZ) for solid state fuel cells. This result does not agree with earlier electrical conductivity data for $(Hf_{1/3}Ce_{1/3}Zr_{1/3})_{1-x}(Gd_{1/2}Y_{1/2})_xO_{2-x/2}$ [47] and $Zr_{1-x}(Gd_{1/5}Pr_{1/5}Nd_{1/5}Sm_{1/5}Y_{1/5})_xO_{2-\delta}$ ($x = 0.1$ and 0.2) [16] oxide ceramics. The conductivity of $(Hf_{1/3}Ce_{1/3}Zr_{1/3})_{1-x}(Gd_{1/2}Y_{1/2})_xO_{2-x/2}$ at 600 °C was within 4×10^{-4} S/cm which is almost an order of magnitude lower than the conductivity of 8YSZ at the same temperature. It can be assumed that the use of a multicomponent composition and the related solid solution disordering can cause local lattice distortions that are likely to impede oxygen anion migration [47]. The conductivities of the earlier studied $Zr_{0.9}(Gd_{1/5}Pr_{1/5}Nd_{1/5}Sm_{1/5}Y_{1/5})_{0.1}O_{2-\delta}$ and $Zr_{0.8}(Gd_{1/5}Pr_{1/5}Nd_{1/5}Sm_{1/5}Y_{1/5})_{0.2}O_{2-\delta}$ ceramic specimens at temperatures up to 550 °C were also an order of magnitude lower than the electrical conductivity of 8YSZ [16]. It was hypothesized that the difference was caused by the presence of the tetragonal phase in the specimens and/or not optimal content of stabilizing oxides [16].

The electrical conductivity data obtained in this study indicate that in $Zr_{0.818}(Y_{1/5}Gd_{1/5}Ho_{1/5}Er_{1/5}Yb_{1/5})_{0.182}O_{1.909}$ multicomponent crystals, the geometry factor (average ionic radius) predominates over the entropy factor.

4. Summary

Compositionally complex $Zr_{0.818}(Y_{1/5}Gd_{1/5}Ho_{1/5}Er_{1/5}Yb_{1/5})_{0.182}O_{1.909}$ single crystals were grown for the first time using the directional melt crystallization technique in a cold crucible. A nearly uniform distribution of ZrO_2, Y_2O_3, Ho_2O_3, and Er_2O_3 was observed along the length of the crystal. The largest deviations from a homogeneous distribution were observed for the components with the greatest and smallest ionic radii, among the five test trivalent oxides (Gd_2O_3 and Yb_2O_3, respectively). The compositionally complex $Zr_{0.818}(Y_{1/5}Gd_{1/5}Ho_{1/5}Er_{1/5}Yb_{1/5})_{0.182}O_{1.909}$ single crystals had a pseudocubic t'' phase structure, similarly to the binary $Zr_{0.818}R_{0.182}O_{1.909}$ single crystals (R = Y, Gd, Ho, Er, Yb). The lattice parameter of the $Zr_{0.818}R_{0.182}O_{1.909}$ crystals increases linearly with an increase in ionic radius of the stabilizing cation. The experimental value of the lattice parameter and the calculated average ionic radius of trivalent cations in the $Zr_{0.818}(Y_{1/5}Gd_{1/5}Ho_{1/5}Er_{1/5}Yb_{1/5})_{0.182}O_{1.909}$ crystals fit well in this dependence. In contrast to binary crystals, a high dislocation density (10^9 cm^{-2}) was observed in the structure of the multicomponent $Zr_{0.818}(Y_{1/5}Gd_{1/5}Ho_{1/5}Er_{1/5}Yb_{1/5})_{0.182}O_{1.909}$ crystals. This may be due to the presence of different-size rare-earth ions in the cation sublattice. The specific high-temperature conductivity of $Zr_{0.818}(Y_{1/5}Gd_{1/5}Ho_{1/5}Er_{1/5}Yb_{1/5})_{0.182}O_{1.909}$ single crystals was comparable to that of 10YSZ single crystals. The conductivity of binary $Zr_{0.818}R_{0.182}O_{1.909}$ and $Zr_{0.818}(Y_{1/5}Gd_{1/5}Ho_{1/5}Er_{1/5}Yb_{1/5})_{0.182}O_{1.909}$ crystals increased linearly with decreasing stabilizing cation ionic radius (the average trivalent cation ionic radius of multicomponent composition).

Thus, increasing the number of stabilizing components in the solid solution did not lead to any significant complication of the directional melt crystallization process for single crystal growth. Furthermore, in contrast to the results of a number of earlier studies, composition modification did not cause a noticeable conductivity drop over the whole temperature range. The obtained values of electrical conductivity in the multicomponent crystal meet the requirements for solid electrolytes in SOFC. Further experimental studies of crystals containing other possible stabilizing oxide combinations are required for better understanding of composition-related effects. For further optimization of the composition in the design of new promising multicomponent materials, it would be very useful to use theoretical computational research methods such as calculations based on first principles, density functional theory, and molecular dynamics.

CRediT authorship contribution statement

Kulebyakin Alexey: Formal analysis. **Korableva Galina:** Formal analysis. **Komarov B.E.:** Formal analysis. **Chislov Artem:** Formal analysis. **Reu A.A.:** Formal analysis. **Myzina Valentina:** Software, Data curation. **Lomonova Elena:** Writing – review & editing, Project administration, Methodology, Data curation, Conceptualization. **Kuritsyna Irina:** Formal analysis. **Zakharov Denis:** Formal analysis. **Borik Mikhail:** Writing – review & editing, Writing – original draft, Supervision, Project administration, Methodology, Conceptualization. **Tapero Maxim:** Formal analysis. **Agarkov Dmitriy:** Formal analysis. **Tabachkova Nataliya:** Writing – review & editing, Writing – original draft, Visualization, Supervision, Methodology, Investigation, Formal analysis, Data curation, Conceptualization. **Milovich Filipp Olegovich:** Visualization, Investigation, Formal analysis.

Declaration of Competing Interest

The authors (D.A. Agarkov, M.A. Borik, A.S. Chislov, B.E. Komarov, G.M. Korableva, A.V. Kulebyakin, I.E. Kuritsyna, E.E. Lomonova, F.O. Milovich, V.A. Myzina, A.A. Reu, N.Y. Tabachkova, M.K. Tapero, D.M.

Zakharov) declare that they have no known competing financial interests or personal relationships that could have appeared to influence the work reported in this paper.

Acknowledgements

This work was financially supported by the Moscow Polytechnic University within the framework of the grant named after Pyotr Kapitsa.

Data availability

Data will be made available on request.

References

[1] J.-W. Yeh, S.-K. Chen, S.-J. Lin, J.-Y. Gan, T.-S. Chin, T.-T. Shun, et al., Nanostructured high-entropy alloys with multiple principal elements: novel alloy design concepts and outcomes, Adv. Eng. Mater. 6 (5) (2004) 299, https://doi.org/10.1002/adem.200300567.

[2] B. Cantor, I.T.H. Chang, P. Knight, A.J.B. Vincent, Microstructural development in equiatomic multicomponent alloys (1–2 SPEC. ISS.):213–8, Mater. Sci. Eng. A (2004) 375–377, https://doi.org/10.1016/j.msea.2003.10.257.

[3] D.B. Miracle, O.N. Senkov, A critical review of high entropy alloys and related concepts, Acta Mater. 122 (2017) 448–511, https://doi.org/10.1016/j.actamat.2016.08.081.

[4] C. Oses, C. Toher, S. Curtarolo, High-entropy ceramics, Nat. Rev. Mater. 5 (2020) 295–309, https://doi.org/10.1038/s41578-019-0170-8.

[5] M.C. Gao, D.B. Miracle, D. Maurice, X. Yan, Y. Zhang, J.A. Hawk, High-entropy functional materials, J. Mater. Res. 33 (19) (2018) 3138–3155, https://doi.org/10.1557/jmr.2018.323.

[6] C.M. Rost, E. Sachet, T. Borman, A. Moballegh, E.C. Dickey, D. Hou, J.L. Jones, S. Curtarolo, J.P. Maria, Entropy-stabilized oxides, Nat. Commun. 6 (2015) 8485, https://doi.org/10.1038/ncomms9485.

[7] A. Sarkar, L. Velasco, D. Wang, Q. Wang, G. Talasila, L. de Biasi, et al., High entropy oxides for reversible energy storage, Nat. Commun. 9 (2018) 3400, https://doi.org/10.1038/s41467-018-05774-5. PMID: 30143625.

[8] C. Zhao, F. Ding, Y. Lu, L. Chen, Y.-S. Hu, High-entropy layered oxide cathodes for sodium-ion batteries, Angew. Chem. 59 (2020) 264–269, https://doi.org/10.1002/anie.201912171.

[9] A. Sarkar, Q. Wang, A. Schiele, M.R. Chellali, S.S. Bhattacharya, D. Wang, T. Brezesinski, H. Hahn, L. Velasco, B. Breitung, High-entropy oxides: fundamental aspects and electrochemical properties, Adv. Mater. 31 (2019) 1806236, https://doi.org/10.1002/adma.201806236.

[10] J. Dąbrowa, M. Stygar, A. Mikuła, A. Knapik, K. Mroczka, W. Tejchman, et al., Synthesis and microstructure of the (Co,Cr,Fe,Mn,Ni)$_3$O$_4$ high entropy oxide characterized by spinel structure, Mater. Lett. 216 (2018) 32–36, https://doi.org/10.1016/j.matlet.2017.12.148.

[11] M. Stygar, J. Dąbrowa, M. Moździerz, M. Zajusz, W. Skubida, K. Mroczka, K. Berent, K. Świerczek, M. Danielewski, Formation and properties of high entropy oxides in Co-Cr-Fe-Mg-Mn-Ni-O system: novel (Cr, Fe, Mg, Mn, Ni)$_3$O$_4$ and (Co, Cr, Fe, Mg, Mn)$_3$O$_4$ high entropy spinels, J. Eur. Ceram. Soc. 40 (4) (2020) 1644–1650, https://doi.org/10.1016/j.jeurceramsoc.2019.11.030.

[12] Y. Ma, Yu Ma, Q. Wang, S. Schweidler, M. Botros, T. Fu, H. Hahn, T. Brezesinski, B. Breitung, High-entropy energy materials: challenges and new opportunities, Energy Environ. Sci. 14 (2021) 2883–2905, https://doi.org/10.1039/D1EE00505G.

[13] M. Anandkumar, E. Trofimov, Synthesis, properties, and applications of high-entropy oxide ceramics: current progress and future perspectives, J. Alloy. Compd. 960 (2023) 170690, https://doi.org/10.1016/j.jallcom.2023.170690.

[14] S. Akrami, P. Edalati, M. Fuji, K. Edalati, High-entropy ceramics: review of principles, production and applications, Mater. Sci. Eng. R. 146 (2021) 100644, https://doi.org/10.1016/j.mser.2021.100644.

[15] A.J. Wright, Q. Wang, C. Huang, A. Nieto, R. Chen, J. Luo, From high-entropy ceramics to compositionally-complex ceramics: a case study of fluorite oxides, J. Eur. Ceram. Soc. 40 (5) (2020) 2120–2129, https://doi.org/10.1016/j.jeurceramsoc.2020.01.015.

[16] A. Kabir, B. Lemieszek, M. Varenik, V.B. Tinti, S. Molin, I. Lubomirsky, V. Esposito, F. Kern, Enhanced mechanical and electromechanical properties of compositionally complex zirconia Zr1−x(Gd1/5Pr1/5Nd1/5Sm1/5Y1/5)xO2−δ ceramics, ACS Appl. Mater. Interfaces 16 (2024) 12765–12772, https://doi.org/10.1021/acsami.3c17501.

[17] L. Spiridigliozzi, C. Ferone, R. Cioffi, G. Dell'Agli, A simple and effective predictor to design novel fluorite-structured high entropy oxides (HEOs), Acta Mater. 202 (2021) 181–189, https://doi.org/10.1016/j.actamat.2020.10.061.

[18] W. Pan, S.R. Phillpot, C. Wan, A. Chernatynskiy, Z. Qu, Low thermal conductivity oxides, MRS Bull. 37 (2012) 917–922, https://doi.org/10.1557/mrs.2012.234.

[19] J.A. Kilner, Ionic conductors: feel the strain, Nat. Mater. 7 (2008) 838–839, https://doi.org/10.1038/nmat2314.

[20] J. Gild, M. Samiee, J.L. Braun, T. Harrington, H. Vega, P.E. Hopkins, K. Vecchio, J. Luo, High-entropy fluorite oxides, J. Eur. Ceram. Soc. 38 (2018) 3578–3584, https://doi.org/10.1016/j.jeurceramsoc.2018.

[21] J. Lang, K. Ren, Y. Wang, Probing the long-term thermal stability mechanism of multi-rare-earth oxide-doped zirconia for solid oxide fuel cell electrolyte, J. Eur. Ceram. Soc. 44 (14) (2024) 116681, https://doi.org/10.1016/j.jeurceramsoc.2024.116681.

[22] M. Pianassola, M. Alexander, B. Chakoumakos, M. Koschan, C. Melcher, M. Zhuravleva, Effects of composition and growth parameters on phase formation in multicomponent aluminum garnet crystals, Acta Crystallogr. Sect. B Struct. Sci. Cryst. Eng. Mater. 78 (3) (2022) 476–484, https://doi.org/10.1107/S2052520622002967.

[23] M. Pianassola, M. Loveday, B.C. Chakoumakos, M. Koschan, C.L. Melcher, M. Zhuravleva, Crystal growth and elemental homogeneity of the multicomponent rare-earth garnet ($Lu_{1/6}Y_{1/6}Ho_{1/6}Dy_{1/6}Tb_{1/6}Gd_{1/6})_3Al_5O_{12}$, Cryst. Growth Des. 20 (10) (2020) 6769–6776, https://doi.org/10.1021/acs.cgd.0c00887.

[24] M. Pianassola, M. Loveday, R. Lalk, K. Pestovich, C.L. Melcher, M. Zhuravleva, Crystal growth and phase formation of high-entropy rare-earth monoclinic aluminates, J. Am. Ceram. Soc. 106 (2023) 7123–7132, https://doi.org/10.1111/jace.19320.

[25] C. Kinsler-Fedon, Q. Zheng, Q. Huang, E.S. Choi, J. Yan, H. Zhou, D. Mandrus, V. Keppenset, Synthesis, characterization, and single-crystal growth of a high-entropy rare-earth pyrochlore oxide, Phys. Rev. Mater. 4 (10) (2020) 104411, https://doi.org/10.1103/PhysRevMaterials.4.104411.

[26] C. Kinsler-Fedon, L. Nuckols, C.T. Nelson, Z. Qi, Q. Huang, D. Mandrus, Y. Zhang, W.J. Weber, V. Keppens, Effects of Au2+irradiation induced damage in a high-entropy pyrochlore oxide single crystal, Scr. Mater. 220 (2022) 114916, https://doi.org/10.1016/J.SCRIPTAMAT.2022.114916.

[27] L.A. Pressley, H.K. Vivanco, T. Berry, M.A. Siegler, T.M. McQueen, Transition metal (dis) order in single crystal multicomponent rare earth perovskites, J. Cryst. Growth 617 (2023) 127262, https://doi.org/10.1016/j.jcrysgro.2023.127262.

[28] M. Pianassola, K.L. Anderson, J. Safin, C. Agca, J.W. McMurray, B. C. Chakoumakos, J.C. Neuefeind, C.L. Melcher, Tuning the melting point and phase stability of rare-earth oxides facilitates their crystal growth from the melt, J. Adv. Ceram. 11 (9) (2022) 1479–1490, https://doi.org/10.1007/s40145-022-0625-z.

[29] H. Peng, X. Ma, W. Yang, Z. Lin, Y. Zheng, Z. Sun, H. Song, Y. Zhang, B. Kang, R. Jia, Z. Feng, S. Cao, Spin switching and magnetocaloric effect of high-entropy orthoferrite single crystal, Ceram. Int 50 (18) (2024) 32288–32294, https://doi.org/10.1016/j.ceramint.2024.06.036.

[30] M.A. Borik, D.M. Zaharov, A.V. Kulebyakin, I.E. Kuritsyna, E.E. Lomonova, N. A. Larina, F.O. Milovich, V.A. Myzina, P.A. Ryabochkina, N.Y. Tabachkova, N. V. Andreev, A.S. Chislov, Single crystal solid state electrolytes based on yttria, ytterbia and gadolinia doped zirconia, Mater. Chem. Phys. 277 (2022) 125499, https://doi.org/10.1016/j.matchemphys.2021.125499.

[31] R.D. Shannon, Revised effective ionic radii and systematic studies of interatomic distances in halides and chalcogenides, Acta Crystallogr 32 (1976) 751–767.

[32] V.V. Osiko, M.A. Borik, E.E. Lomonova, Synthesis of Refractory Materials by Skull Melting. In Springer handbook of crystal growth., Springer, New York, 2010, pp. 433–477, https://doi.org/10.1007/978-3-540-74761-1_14.

[33] X. Tan, S. Xu, F. Liu, X. Wang, B.A. Goodman, D. Xiong, W. Deng, Highly efficient up-conversion green emission in Ho/Yb co-doped yttria-stabilized zirconia single crystals, J. Lumin 209 (2019) 95–101, https://doi.org/10.1016/j.jlumin.2019.01.041.

[34] X. Wang, X. Tan, S. Xu, F. Liu, B.A. Goodman, W. Deng, Preparation and up-conversion luminescence of Er-doped yttria stabilized zirconia single crystals, J. Lumin 219 (2020) 116896, https://doi.org/10.1016/j.jlumin.2019.116896.

[35] Z. Sun, N. Renfro, A.C. Palke, Tri-color-change holmium-doped synthetic CZ, Gems Gemol. 53 (2) (2017) 259–260.

[36] K. Chen, J. Ma, C. Tan, C. Li, L. An, An anion-deficient high-entropy fluorite oxide with very low density, Ceram. Int 47 (2021) 21207–21211, https://doi.org/10.1016/j.ceramint.2021.04.123.

[37] X. Ping, Q. Yang, B. Meng, Z. Ma, X. Pan, Structural, thermophysical, mechanical and electrical properties of equimolar five-principal element fluorite-structured high-entropy oxides, J. Alloy. Compd. 975 (2024) 172971, https://doi.org/10.1016/j.jallcom.2023.172971.

[38] Y. Hemberger, N. Wichtner, C. Berthold, K.G. Nickel, Quantification of yttria in stabilized zirconia by Raman spectroscopy, Int J. Appl. Ceram. Technol. 13 (2016) 116–124, https://doi.org/10.1111/ijac.12434.

[39] M. Yashima, S. Sasaki, M. Kakihana, Y. Yamaguchi, H. Arashi, M. Yoshimura, Oxygen-induced structural-change of the tetragonal phase around the tetragonal-cubic phase-boundary in ZrO_2-$YO_{1.5}$ solid-solutions, Acta Crystallogr B Struct. Sci. 50 (1994) 663–672, https://doi.org/10.1107/S0108768194006257.

[40] M. Yashima, K. Ohtake, M. Kakihana, H. Arashi, M. Yoshimura, Determination of tetragonal–cubic phase boundary of $Zr_{1-x}R_xO_{2-x/2}$ (R = Nd, Sm, Y, Er and Yb) by Raman scattering, J. Phys. Chem. Solids 57 (1996) 17–24, https://doi.org/10.1016/0022-3697(95)00085-2.

[41] D.M. Lipkin, J.A. Krogstad, Y. Gao, C.A. Johnson, W.A. Nelson, C.G. Levi, Phase evolution upon aging of air plasma spray t'-zirconia coatings: I – synchrotron X-ray diffraction, J. Am. Ceram. Soc. 96 (1) (2013) 290–298, https://doi.org/10.1111/j.1551-2916.2012.05451.x.

[42] M.A. Borik, S.I. Bredikhin, V.T. Bublik, A.V. Kulebyakin, I.E. Kuritsyna, E. E. Lomonova, F.O. Milovich, V.A. Myzina, V.V. Osiko, P.A. Ryabochkina, Tabachkova NYu, T.V. Volkova, The impact of structural changes in ZrO_2-Y_2O_3 solid solution crystals grown by directional crystallization of the melt on their transport characteristics, Mater. Lett. 205 (2017) 186–189, https://doi.org/10.1016/j.matlet.2017.06.059.

[43] J.A. Krogstad, R.M. Leckie, S. Krämer, J.M. Cairney, D.M. Lipkin, C.A. Johnson, C. G. Levi, Phase evolution upon aging of air plasma sprayed t'-zirconia coatings:

II–microstructure evolution, J. Am. Ceram. Soc. 96 (1) (2013) 299–307, https://doi.org/10.1111/j.1551-2916.2012.05460.x.

[44] B. Butz, P. Kruse, H. Störmer, D. Gerthsen, A. Müller, A. Weber, E. Ivers-Tiffée, Correlation between microstructure and degradation in conductivity for cubic Y_2O_3-doped ZrO_2, Solid State Ion. 177 (37) (2006) 3275–3284, https://doi.org/10.1016/j.ssi.2006.09.003Get rights and content.

[45] Y. Han, X. Liu, Q. Zhang, M. Huang, Y. Li, W. Pan, P. Zong, L. Li, Z. Yang, Y. Feng, P. Zhang, C. Wan, Ultra-dense dislocations stabilized in high entropy oxide ceramics, Nat. Commun. 13 (1) (2022) 2871, https://doi.org/10.1038/s41467-022-30260-4.

[46] S. Omar, W.B. Najib, W. Chen, N. Bonanos, Electrical conductivity of 10 mol% Sc2O3–1 mol% M2O3–ZrO2 ceramics, J. Am. Ceram. Soc. 95 (6) (2012) 1965–1972, https://doi.org/10.1111/j.1551-2916.2012.05126.x.

[47] E. Bonnet, J.C. Grenier, J.M. Bassat, A. Jacob, B. Delatouche, S. Bourdais, On the ionic conductivity of some zirconia-derived high-entropy oxides, J. Eur. Ceram. Soc. 41 (8) (2021) 4505–4515, https://doi.org/10.1016/j.jeurceramsoc.2021.03.021.